Energy & Buildings 301 (2023) 113704

Contents lists available at ScienceDirect

Energy & Buildings

journal homepage: www.elsevier.com/locate/enb

Study on predicting the radiant heat flow rate of floor surface of radiant floor heating

Lidi Lu [a,b], Lulin Luo [a,b], Jinhua Chen [a,b,c,*]

[a] Joint International Research Laboratory of Green Buildings and Built Environments (Ministry of Education), Chongqing University, Chongqing, 400045, China
[b] National Centre for International Research of Low-carbon and Green Buildings (Ministry of Science and Technology), Chongqing University, Chongqing, 400045, China
[c] Key Laboratory of the Three Gorges Reservoir Region's Eco-Environment (Ministry of Education), Chongqing University, Chongqing, 400045, China

ARTICLE INFO

Keywords:
Low emissivity
Non-radiative surface
Radiant heat flow rate
Empirical formula
Floor radiant heating
Wall insulation

ABSTRACT

Radiant heat flow rate of radiant surface is crucial for radiant floor heating design and terminal selection. We found that the present empirical formula to predict radiant heat flow rate of radiant surface has limits under varied room size and surface emissivity circumstances. Wall insulation conditions also have substantial influences on the operating efficiency of floor radiant heating. Adopting machine learning algorithms and backward selection method, a two-layer Neural Network model was demonstrated to have good accuracy and requisite relevant features for new empirical formula was identified. The new formula containing the information of room depth, weighted radiant surface area, insulation conditions, indoor air temperature and radiant surface temperature as independent variables exhibits great accuracy with R-squared of 0.97 and *RMSE* of 2.74. The substitution of *AUST* with indoor air temperature can increase the prediction accuracy. Analysis reveals structural pattern and indicates interaction between wall insulation and non-radiative surface with low emissivity. We propose the use of non-radiant surfaces with low emissivity as a passive energy-saving technique for radiant floor heating. And the updated empirical formula can increase its application scenarios, and aid promote application of FRH and new passive technique.

1. Introduction

Heating, ventilation, and air conditioning (HVAC) systems account for approximately 40 percent of building energy consumption [1]. As people's awareness of energy conservation and environmental protection increases, creating thermal comfortable indoor environments in a more energy-efficient manner is becoming increasingly valued. One strategy for conserving energy is to improve the heat transfer performance of the air conditioning terminal [2]. For the selection and design of HVAC equipment, predicting heat transfer performance is crucial. The radiant floor heating (FRH) can provide superior thermal comfort and system energy savings [3–5] and hence has foreseeable application prospects. ASHRAE handbook [6] and *Technical specification for radiant heating and cooling* (JGJ 142) [7] have provide empirical formulas for predicting the convective and radiant heat flow rate of floor surface for FRH.

Several studies have demonstrated that the heat transfer performance of radiant air conditioning (RAC) is dependent on the structure of the building envelope and outdoor conditions, and energy-saving research is increasingly concentrating on the interaction between the building envelope and the air conditioner. Wall insulation is being developed with the purpose of lowering the energy consumption of HAVC. Internal insulation on exterior walls is more conducive to intermittent operation than external insulation, according to [8], because the former corresponds to a faster rate of temperature rise. At the start of intermittent operation, however, the indoor air temperature in the internal insulation room is slightly lower than that in the external insulation room. Intermittent operation can reduce air conditioning demand by 44–55 % compared to continuous operation, and internal insulation on walls saves 7–19 % more energy than external insulation [9,10]. Adding insulation to interior walls has an energy-saving effect as well. According to a study of a residential building in hot summer and cold winter region of China, this method can reduce annual air conditioning demand by 2.41–25.31 % [11], with thicker insulation layer preferable. However, another study suggests that when the insulation thickness is increased to 35 mm or more, the energy efficiency growth rate in rooms heated by radiation is less than 5 % [12]. According to Cvetkovi's research [13], the radiant air-conditioned room with the optimal insulation layer thickness is significantly more energy-efficient

* Corresponding author at: Chongqing University, Chongqing, 400045, China.
E-mail address: cjh@cqu.edu.cn (J. Chen).

https://doi.org/10.1016/j.enbuild.2023.113704
Received 16 August 2023; Received in revised form 7 October 2023; Accepted 26 October 2023
Available online 29 October 2023

Nomenclature

Acronyms

HVAC	Heating, ventilation, and air conditioning
FRH	Floor Radiant Heating
RAC	Radiant air conditioning
AC	Air conditioning
ML	Machine learning
XGBoost	eXtreme Gradient Boosting
CART	Classification And Regression Tree
GPR	Gaussian Process Regression
SVM	Support Vector Machine
NN	Neural Network
AUST	Area-weighted unheated surface temperature
RMSE	Root mean squared error
VIF	Variance inflation factor
PCA	Principal component analysis
NLS	Nonlinear Least Squares
MRT	Mean radiant temperature
q_r	Radiant heat flow rate of floor surface (W/m^2)
t_p	Radiant surface temperature (°C)
t_a	Indoor air temperature (°C)
I	Insulated areas of interior wall (m^2)
R	Insulated areas of roof (m^2)
X	View factor
E	Emissivity
A	Area of the surface (m^2)
A_ε	Area weighted coefficient
F	Undetermined coefficient
ΔK	Temperature difference between radiant surface and indoor air (°C)
D	Depth of the room (m)

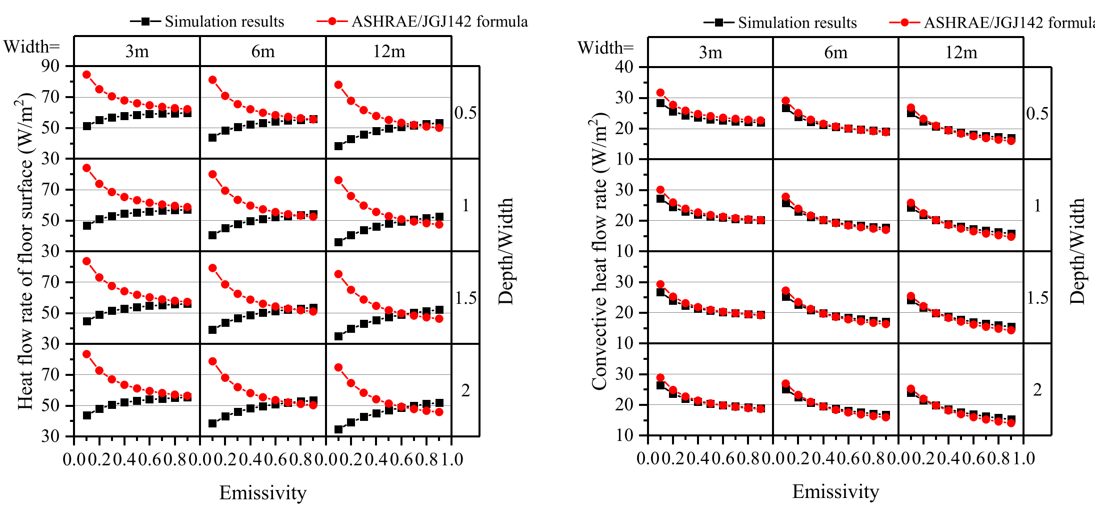

(a) Total heat flow rate of floor surface

(b) Convective heat flow rate of floor surface

Fig. 1. Comparison of heat flow rate of floor surface.

than that with conventional insulation layer. In addition to placing insulation on vertical walls, Xiao [14] discovered by simulation that roof insulation had a greater energy-saving benefit than exterior wall insulation. Some research [15–19] have shown that decreasing the non-radiative surface emissivity can boost the thermal comfort of radiant heating and cooling, which is regarded to have energy-saving potential. Room size also affects the operational effects of HVAC, and numerous applications of radiation air conditioning on airports [20,21] and churches [22] have proven its superiority for large space building. Low emissivity surface can also efficiently shorten the response time of FRH and minimize its energy requirement at starting period, according to our preliminary research. The surfaces of the objects serve as the medium for radiative heat transmission, and differences in their surface area, spatial position, and emissivity can affect the radiant heat transfer process. In order to optimize the operational performance of radiation air conditioning, it is crucial to pay special attention to the condition of the inner surface of building envelops.

The heat flow rate of floor surface is a crucial criterion for selecting FRH terminals. Existing empirical formulas can no longer accurately predict the heat transfer performance of FRH [19,23] due to the diversification of radiation air conditioning application circumstances, such as different room size and novel passive techniques of low-emissivity non-radiative surface. Consequently, it is necessary to develop improved formulas or models to predict the heat transfer performance of FRH during actual operation in more complex scenarios, providing designers with a basis for equipment selection, which is crucial for ensuring the efficacy of building energy-saving engineering.

With the development of computer science and technology, the use of machine learning (ML) algorithms for evaluating building performance and controlling equipment operation has increased significantly [24,25]. Zhang [26] evaluated the errors used for advanced control of HAVC by employing six typical ML methods and historical thermal data from the building. Results indicate that Bayesian Neural Networks (NN) and probabilistic ensemble NN exhibit superior performance [27]. Partial Least Squares regression models can predict the risk of mould growth in wooden frame walls under different climatic conditions, including temperature, rainfall, and solar radiation [28]. Utilizing of extreme learning machine to predict heat transfer coefficient and building heat loss, particularly at the junction of window frames and walls, can facilitate design optimization [29]. Multi-layer NN can be used to monitor the ventilation and airtightness of buildings [30]. Shen [31] compared the performance of extreme gradient boosting (XGBoost)

Table 1
Multicollinearity diagnosis results.

Independent variable	Tolerance	VIF	Remarks
$E-1$	1.0	1.0	keep
$E-2$	1.0	1.0	keep
$E-3$	1.0	1.0	keep
$E-4$	1.0	1.0	keep
$X_{6,4}$	0.875	1.143	keep
$T_{Boundary}$	0.875	1.143	keep
$A_{1/All}$	7.6×10^{-6}	1.3×10^{5}	collinear
$A_{2/All}$	7.6×10^{-6}	1.3×10^{5}	collinear
$A_{3/All}$	7.6×10^{-6}	1.3×10^{5}	collinear
$A_{4/All}$	7.6×10^{-6}	1.3×10^{5}	collinear
$X_{6,1}$	6.5×10^{-6}	1.5×10^{5}	collinear
$X_{6,2}$	4.5×10^{-14}	2.2×10^{13}	collinear
$X_{6,3}$	6.7×10^{-5}	1.5×10^{4}	collinear

Note: In the table, $T_{Boundary}$ is the external boundary temperature of the indoor partition wall; alphabet E, X and A designate surface emissivity, view factor, and proportion of an area, respectively; number 1,2,3 and 4 represent inner surface of external wall, household partition wall, indoor partition wall, and the roof respectively; $I-2$, $I-3$, and $I-4$ are categorical variables and do not participate in multicollinearity diagnosis.

and deep NN in predicting the heat flux of various building structures in order to reduce the computational expense of building energy management. Chen [32] proposed an optimized control strategy for FRH systems based on a thermal response time prediction model utilizing the Gaussian process regression (GPR) algorithm, which can effectively reduce the thermal response time of floor radiation heating systems and improve indoor thermal comfort during the thermal response phase without compromising energy consumption. In brief, application of a suitable machine learning algorithm can aid in achieving the objective of energy conservation in buildings.

This paper employs appropriate ML algorithms to develop a regression model for the unit area radiant heat flow rate of FRH's floor surface, as well as the backward selection method to identify necessary relevant features and infer the structure of a reasonable prediction formula, thereby expanding its application scenarios.

2. Modeling/methodology

Nowadays, the development of computer science allows researchers to train predictive models using ML algorithms. Some complex measurement and calculation procedures can be replaced by ML algorithms in order to achieve engineering goals with greater efficiency and precision. Whereas, in engineering practice, concise and straightforward formulas are more practical and convenient. In this paper, employs data gathered from prior work are employed for ML training, and the details of the model based on can be found in the Appendix A.

Analysing a second set of data gathered from an earlier simulation study [19] demonstrates that, as room size increases, the present empirical formula calculation results become progressively less than the simulation findings, as depicted in Fig. 1. In response to a drop in non-radiative surface emissivity, the formula calculation results surpass the simulation findings, which may lead to an underestimating of the FRH's layout area and a reduction in its heating effect. Fig. 1 (b) demonstrates that the convective heat flow rate of floor surface predicted by the ASHRAE formula is comparable to the simulation results, therefore it can be concluded that the radiant heat flow rate of floor surface q_r exhibited the greatest variance. Therefore, the primary aim of this paper is to improve prediction method of q_r.

2.1. Select appropriate machine learning model

ML is a subfield of artificial intelligence that uses data to learn the relationship between the quantities of interest in order to gain insight into the system's operation and predict the unobserved quantities [33]. The properties of the data and the information to be predicted determine which ML model is most appropriate for each problem. For labeled training data, models such as support vector machines (SVM), classification and regression tree (CART), and NN can be used to supervise the learning process. For a brief introduction, CART is a supervised learning approach that constructs a decision tree to make predictions [34]; GPR is a nonparametric model that employs Gaussian Process (GP) prior to doing data regression analysis. This model's solution is based on Bayesian inference and assumes two components: noise (regression residual) and GP prior [35]; SVM is a technique for supervised learning that maximizes the classification interval by locating a hyperplane for classification or regression [36]. NN have been in existence since the 1950s, but it's not until recent years that significant progress is made in this technology due to improvements in computing power and training methods, and widely used in civil engineering tasks [27].NN is a mathematical model that simulates the structure and operation of neural networks in the human brain. It is made of several brain nodes and conveys data via connection weights [37].

When selecting ML models, one must consider both the accuracy of the model's predictions and the training time. Hyperparameters are external configuration variables used to manage model training, and are essential for ML because they control the model's structure, functionality, and performance directly. [38]. One of the hyperparameters that users can debug is the kernel function. The kernel function for SVM consists of a quadratic kernel, a cubic kernel, and a Gaussian kernel. Gaussian kernel can be further subdivided based on its hyperparameters into coarse Gaussian, medium Gaussian, and fine Gaussian. Different hyperparameters provide the classification of NN as narrow neural networks, medium neural networks, and broad neural networks. For other hyperparameters, the number of layers, the size of each layer, and the activation function connecting each layer are included, using NN as an example. By attempting various hyperparameter optimizations, it is possible to achieve satisfactory prediction results.

To examine the predictive performance of ML models, R-squared (R^2) and the root mean squared error (*RMSE*) metrics are employed in this paper, and the methods of calculation are shown as Eq. (1) and (2). In order to increase the model's generalization capacity and prevent overfitting, the dataset is split into training and testing sets in a 7:3 ratio, and an 8-fold cross validation is conducted. The testing set is a dataset used to evaluate the performance of a model that is completely independent of the training set and is used to test the performance of the model on new data. Cross validation set is also a method used to evaluate model performance by dividing the data into k subsets, then using the $k-1$ subset as the training set in each iteration, and the remaining 1 subset as the validation set to evaluate model performance. This procedure is done k times, with a different subset serving as the validation set each time. Finally, the performance of the model is determined by averaging the outcomes of k iterations.

$$R^2(y,\hat{y}) = 1 - \frac{\sum_{i=0}^{n-1}(y_i-\hat{y}_i)^2}{\sum_{i=0}^{n-1}(y_i-\bar{y})^2} \tag{1}$$

where, $\hat{y}_i$ ——Corresponding predicted value of y_i; $\bar{y}$——Mean value of true dataset.

$$RMSE = \sqrt{\frac{\sum_{i=1}^{n}(y_i-\hat{y}_i)^2}{n}} \tag{2}$$

The computer configuration used to train the model is as follows: Intel Core i5-8400@2.80 GHz (6 core CPUs), NVIDIA GTX 1060 3G (GPU), 8 + 16 GB DDR3@4400 MHz RAM (RAM).

Table 2
Evaluation results of different machine learning regression models.

	SVM	CART	GPR	NN
R-square (verify)	1.00	0.99	1.00	1.00
R-square (test)	1.00	1.00	1.00	1.00
R-square (9 m test)	0.69	0.97	0.62	1.00
RMSE (verify)	1.265	1.656	0.633	0.778
RMSE (test)	1.209	1.154	0.558	0.678
RMSE (9 m test)	−0.01	1.062	3.871	0.206
Training time	47.9 s	2.4 s	29.2 s	8.8 s

2.2. Identify essential relevant features

It is essential to select suitable features. The characteristics that contribute to the model are referred to as “relevant features”, while those that do not are referred to as “irrelevant features”. Excessive characteristics can result in the curse of dimensionality, which doubles the computing complexity. Each machine learning sample has numerous characteristics. In addition to radiant surface temperature t_p, air temperature t_a, and area-weighted unheated surface temperature (*AUST*), features for predicting q_r include room size, emissivity of each unheated surface, wall insulation method, and neighboring room boundary temperature information.

The multicollinearity diagnosis is utilized to preliminarily filter features. Multicollinearity is the linear relationship between numerous parameters inside a model of multiple regression. Multicollinearity issues may emerge if there is a high correlation between multiple factors. It is crucial to test for multicollinearity because multicollinearity might reduce the predictive potential of a model. Typical techniques for measuring multicollinearity include the correlation coefficient matrix R test of independent variables, the variance inflation factor (VIF) test, and the eigenvalue test. In this paper, the VIF test is used as the assessment method. The higher the VIF score, the stronger the relationship between independent variables. If the value of the VIF is more than 10, a serious multicollinearity problem develops.

Table 1 displays the multicollinearity diagnostic results of the independent variables, where the VIF of the independent factors linked to emissivity is less than 5, however the independent variables related to area and spatial position indicate severe collinearity. This phenomenon is rational, as the geometric shapes and parameters abstracted from the room, which are dictated by the dimensions of the three most fundamental dimensions, determine the view factors representing the relative positions of diverse surface spaces. When the width and net height of a room are fixed, the depth of the space is the only variable that determines the other dimensions. After determining the origin of the multicollinearity phenomena, it is possible to determine which features must be kept when employing candidate features for linear regression or machine learning regression. However, some filtered features are not mutually exclusive with the retained features, but rather have substitutable relationships. For example, replacing $X_{6,4}$ (view factor of radiation surface to roof) with $A_{4/All}$ (proportion of the roof to the area of all non-radiative surfaces) will not significantly affect the accuracy of the regression model, because there is no significant difference in the utility of the two variables in the model. Considering that surface emissivity and surface area are important for radiant heat transfer, an area weighted coefficient, designated A_ε, is determined from the first two by referring the calculation technique of weighting coefficients in *AUST*. The formula for this calculation is as follows:

$$A_{\varepsilon,i} = \frac{\varepsilon_i A_i}{\sum_{n=1}^{6} \varepsilon_n A_n} \tag{3}$$

When interpretability of the model is not needed, ML algorithms can employ principal component analysis (PCA) to minimize the dimensionality of data. The resultant principal component is a linear combination of all original features; when interpretability of the model is considered, the backward selection method can be used to choose features. This method begins with the model including all features, removes feature variables progressively, and continues until deleting the remaining feature variables does not enhance the model’s fit considerably. This paper uses the backward selection to choose its features.

2.3. Infer the structure and coefficients of empirical formula

The empirical formula in JGJ 142 must be logical within particular constraints. Considering the structure of q_r, we can record the structure and coefficients of the new prediction formula as follows:

$$q_r' = F_a \times \left[(t_p + 273)^4 - (AUST + 273)^4 \right] \tag{4}$$

In Eq. (4), F_a is the undetermined coefficient. Although *AUST* has a clear technique of computation, it is difficult to estimate the temperature of each surface. Therefore, try to substitute t_a for *AUST*, and get Eq. (5):

$$q_r' = F_b \left[(t_p + 273)^4 - (t_a + 273)^4 \right] \tag{5}$$

In Eq. (5), F_b is the undetermined coefficient, whose value is related to $A_{\varepsilon,i}$, t_a, the temperature difference between the air and the floor surface ($\Delta K = t_p - t_a$), and t_p, namely:

$$F_b = f\left(A_{\varepsilon,1}, A_{\varepsilon,2}, A_{\varepsilon,3}, A_{\varepsilon,4}, A_{\varepsilon,5}, t_a, t_p, \Delta K\right) \tag{6}$$

Solving the coefficients is the key to the prediction formula. Not all input variables in Eq. (6) are required, and the most important tasks is to characterize their connection with each input variable using suitable functions.

This part’s objective is to determine F_b, as the prediction formula is not an analytical formula generated from theory, but rather a data-driven empirical form. Firstly, using primary effects analysis, identify the influence of the input variable on F_b. Secondly, using the Nonlinear Least Squares (NLS) technique, develop the final functional connection. Origin (a professional data analysis software) incorporates the Levenberg-Marquardt approach for NLS fitting of nonlinear functions. This methodology quickly identifies the ideal value by combining the steepest descent and linearization methods (Taylor series). Origin is used to implement the algorithm in this section.

3. Results and analysis

3.1. Performance of machine learning regression models for prediction

It is necessary to try various different regression models and compare their performance to ultimately select the optimal model. This section uses a regression learner in MATLAB to establish a machine learning regression model. When 13 features are selected, including room depth, boundary temperature, external wall insulation method, internal wall insulation method, t_a, t_p, ΔK, and A_ε of the 6-sided envelop surfaces.

The 1536 data sets from Appendix A are divided into two categories, with 3 m, 6 m, and 12 m depth data used for machine learning. Among them, 12.5 % of the data is randomly selected to form the test set, and the remaining dataset also includes the cross-validation set; The second category is data with the depth of 9 m, which is used to verify the predictive performance of trained models when faced with completely unfamiliar data.

Table 2 displays the evaluation indicators of regression models generated by various machine learning algorithms using the provided data. This is the optimal performance of each algorithm type after adjusting various hyperparameters. The ML algorithms successfully validated by two types of test sets are double-layer NN and fine-tree CART, as observed. Using 9 m data validation, NN has the highest accuracy of the two, while CART’s R^2 decreases to 0.97. The remaining SVM and GPR performed well on the first type test set, but failed the

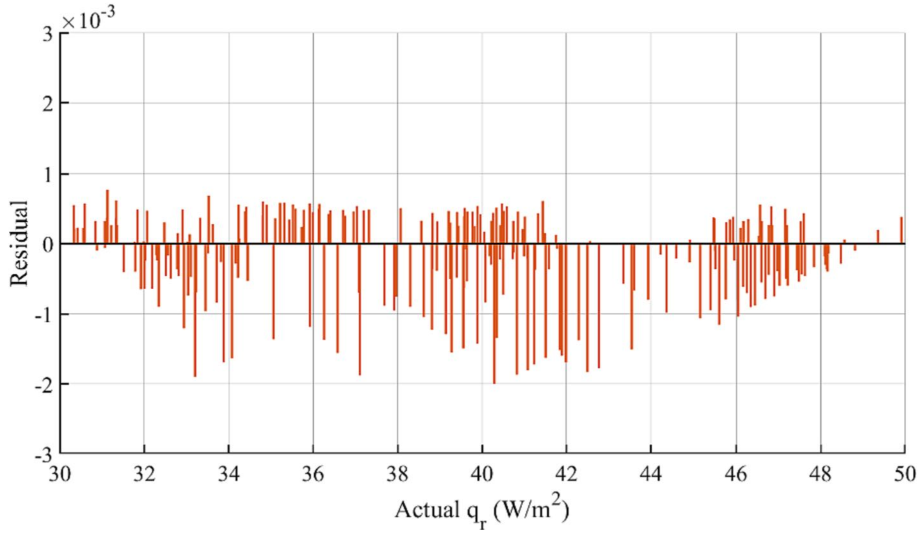

Fig. 2. Residual graph of the two-layer neural network model.

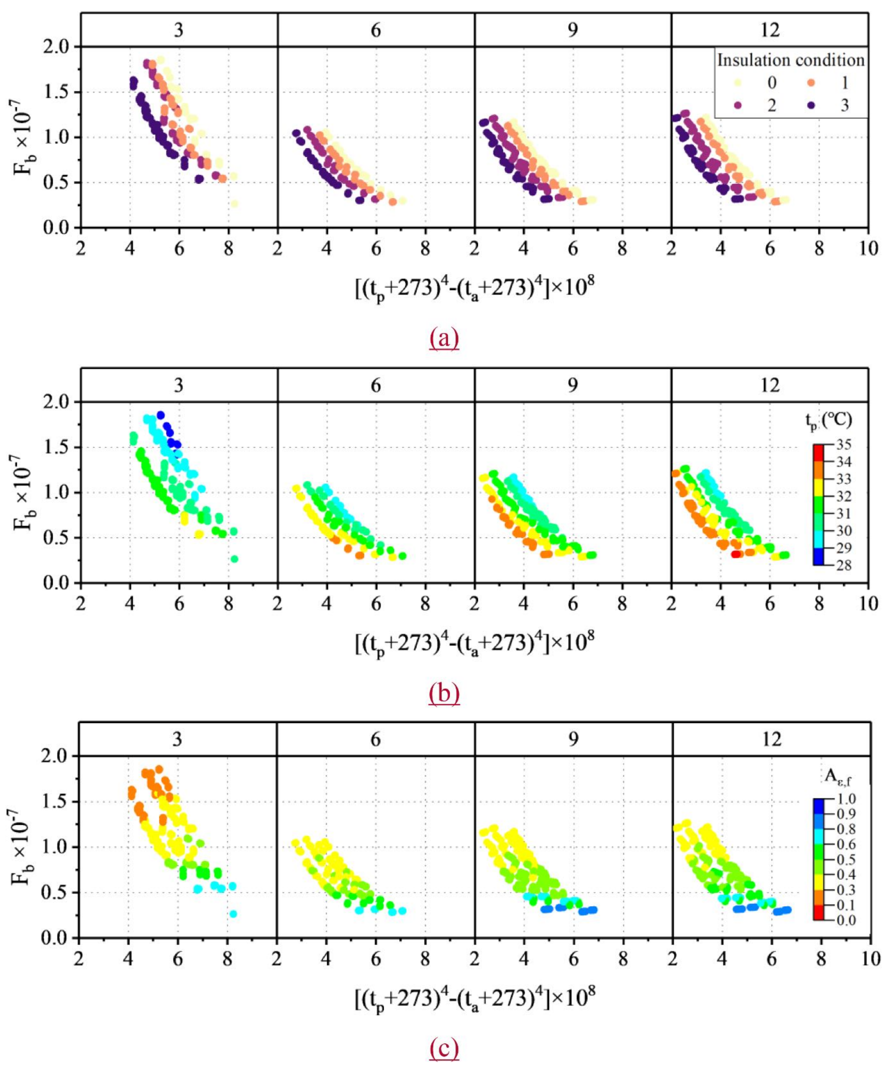

Fig. 3. Scatter plot of coefficient F_b.

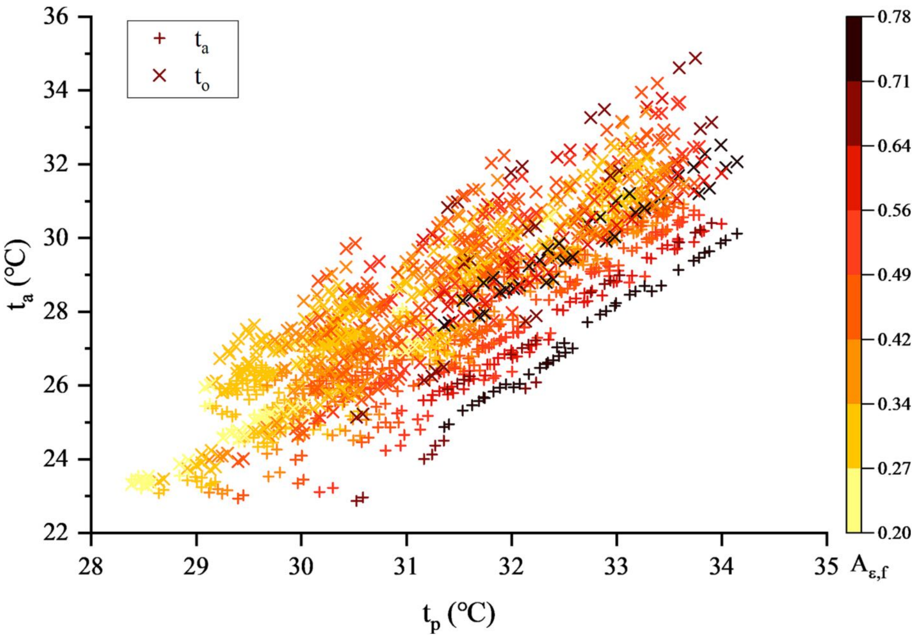

Fig. 4. Scatter graph between t_p and t_a.

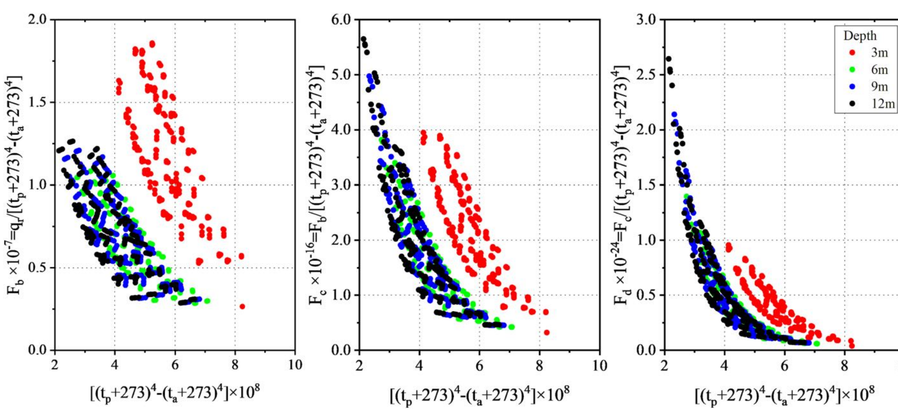

Fig. 5. Scatter plot of exponential decay relationships.

second type test set validation. The identical circumstance exists for single-layer NN, three-layer NN, and rough-tree CART.

Two-layer NN model has the shortest training time and guaranteed prediction performance of the three models, making it the most appropriate model. Therefore, we selected the two-layer NN model and continued to use the backward selection method, ultimately reducing the number of relevant features to four: room depth D, $A_{\varepsilon,6}$, t_p and t_a (or *ASUT*), and then further reduction of features will significantly diminish the predictive performance of the model. When the last feature is picked as t_a, the two-layer NN model has superior prediction performance compared to the model where the last feature is *AUST*, with an *RMSE* from 9 m test set of 0.20 against 1.11, and residual shown in Fig. 2. the residual of the two-layer NN model's prediction residuals are within ± 0.003. To sum up, compared to selecting features as t_p and *AUST*, selecting t_p and t_a improves the prediction accuracy of the model, whereas the measurement difficulty of t_a is lower than that of *AUST*. These findings are particularly valuable for identifying the structure of nonlinear prediction models.

3.2. Structure and coefficients of prediction formula

After establishing the features utilized to concretize q_r through ML algorithm, i.e., the variables of the empirical formula to be calculated, the positions of these variables in pending formula should be inferred. In theory, empirical formulas can approximate implicit analytical formulas in a variety of ways. This paper will only present a trustworthy formula and its derivation.

Firstly, draw the relationship between F_b and ΔK^4_{p-a} ($\Delta K^4_{p-a} = \left[(t_p + 273)^4 - (AUST + 273)^4\right]$) by using the information from Section 2.3 and 3.2. As shown in Fig. 3,there is a pattern between F_b and ΔK^4_{p-a} at different depths of room. The greater the ΔK^4_{p-a}, the less the F_b. Based on the distribution of scattered points, negative power or exponential functions can be utilized to illustrate the relationship between the two. Analyzing the scatter coloring scenario depicted in Fig. 3 (a), it is evident that the data points are clearly segregated into vertically separate function curves by distinct interior wall and roof insulation conditions (for convenience, four insulation conditions are represented by numbers: 0 indicates no insulation, 1 indicates interior wall insulated, 2 indicates roof insulated, and 3 indicates both interior wall and roof insulated). Analogous effects exist with varying concentrations of t_p or t_a, as shown in Fig. 3 (b). From the aforementioned occurrence, it can be deduced that the values of t_p or t_a are influenced by building envelop insulation conditions, and the correlation between the two allows ML

Table 3
Fitting results of exponential function.

Depth	Insulation	a	$k \times 10^{-9}$	R^2
3	0	6.00	−2.65	0.89
	1	5.77	−2.60	0.85
	2	5.50	−2.30	0.84
	3	5.00	−2.00	0.95
6	0	4.70	−2.35	0.98
	1	4.52	−2.32	0.96
	2	4.28	−2.25	0.96
	3	3.96	−2.13	0.98
9	0	4.63	−2.35	0.98
	1	4.45	−2.30	0.96
	2	4.17	−2.26	0.94
	3	3.85	−2.20	0.95
12	0	4.55	−2.30	0.98
	1	4.37	−2.26	0.96
	2	4.07	−2.24	0.94
	3	3.75	−2.17	0.94

models to maintain strong predictive performance even without features involving insulation information. We further confirmed that A_ε, surface emissivity and temperature boundary, cannot differentiate the function curve in the same way that insulation condition does. Using Fig. 3 (c) as an example, the change in the weighted area coefficient of the floor surface $A_{\varepsilon f}$ only changes the specific position of the data points, but cannot distinguish different function curves. However, this does not imply that the change in emissivity has no effect. t_a increases with the decreasing of $A_{\varepsilon f}$ under same level of t_p as shown in Fig. 4, and so does t_o. Fig. 5.

The preceding analysis suggests that the variable representing the area of the insulation wall is necessary. To determine the form of this variable, the NLS method is applied to the 16 curves identified by room depths and wall insulations method in Fig. 3 (a). It indicates that the general form follows exponential functions with natural constant. The deduction is supported by the fact that the feature of the function image of q_r remains consistent regardless of how many times it is divided by ΔK^4_{p-a}, in addition to the evidence of accuracy of fitting results. The general form of exponential function is thus expressed as Eq. (7), and the calculation results including R^2 and different values of coefficients a and k under conditions of varying room depths and insulation conditions are presented in Table 3. The fitting effects are satisfactory with the majority of R^2 are greater than 0.94, except for the data with room depth of 3 m, which have slightly lower R^2 and will be analyzed in discuss section.

$$q_r = exp\left(a + k\left[\left(t_p + 273\right)^4 - \left(t_a + 273\right)^4\right]\right) \quad (7)$$

The association analysis shows that there a correlation between coefficient a and k. As shown in Fig. 6, the data distribution under different depths satisfies logarithmic function, and the function form is marked as Eq. (8). Consequence, coefficients m and n in Eq. (8) are determine with same method and are found linear relationship between the two. At this point, the functional expression of n is computed with independent variable of room depth, as shown in Fig. 7. The same technique was repeated to obtain the functional relationship between n and depth, as shown in Fig. 7.Fig. 8.

$$-k \times 10^9 = ln(ma + n) \quad (8)$$

In the end, only one coefficient a remains undetermined. As depicted in Fig. 9, the concept of symbolic-graphic combination is consistently utilized to determine distribution pattern under various insulation conditions and room depths. Under various depths, the characteristics of the four curves are consistent and approximate linear distribution. However, the issue is that the values 0,1,2,3 representing four types of wall insulation conditions cannot be used directly as variables. To quantify the effect of wall insulation on the formula, it is necessary to consider not only the area of the wall where insulation methods are

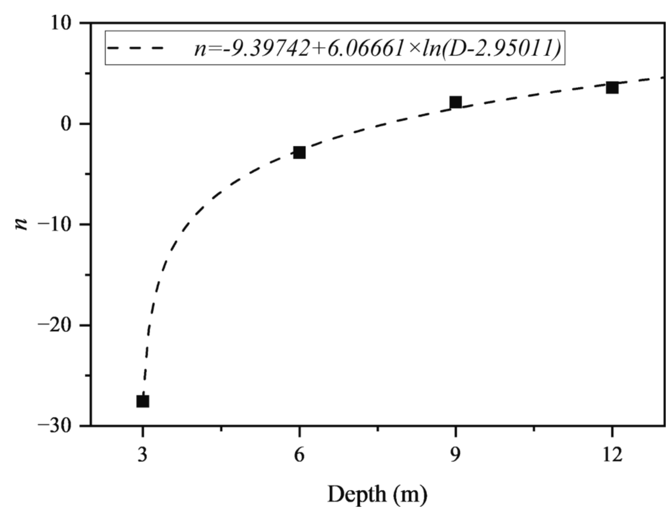

Fig. 7. Coefficient n.

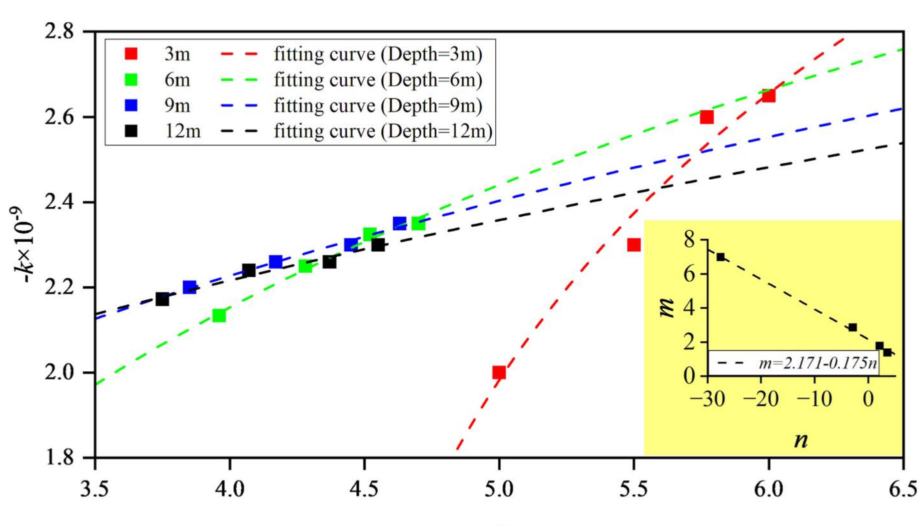

Fig. 6. Logarithmic relationship between coefficient a and k.

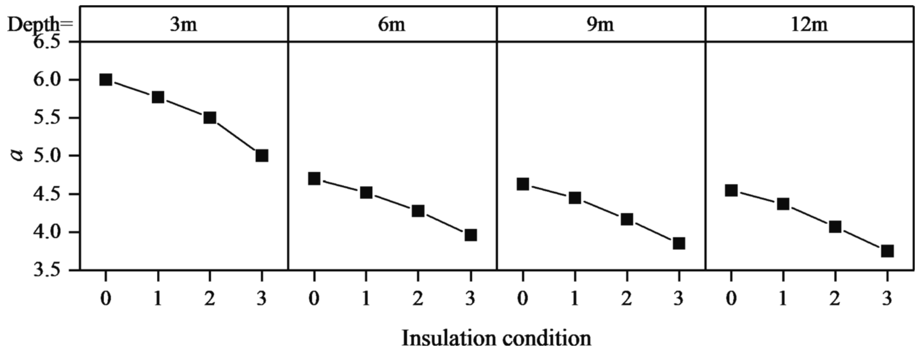

Fig. 8. Coefficient a under different insulation conditions.

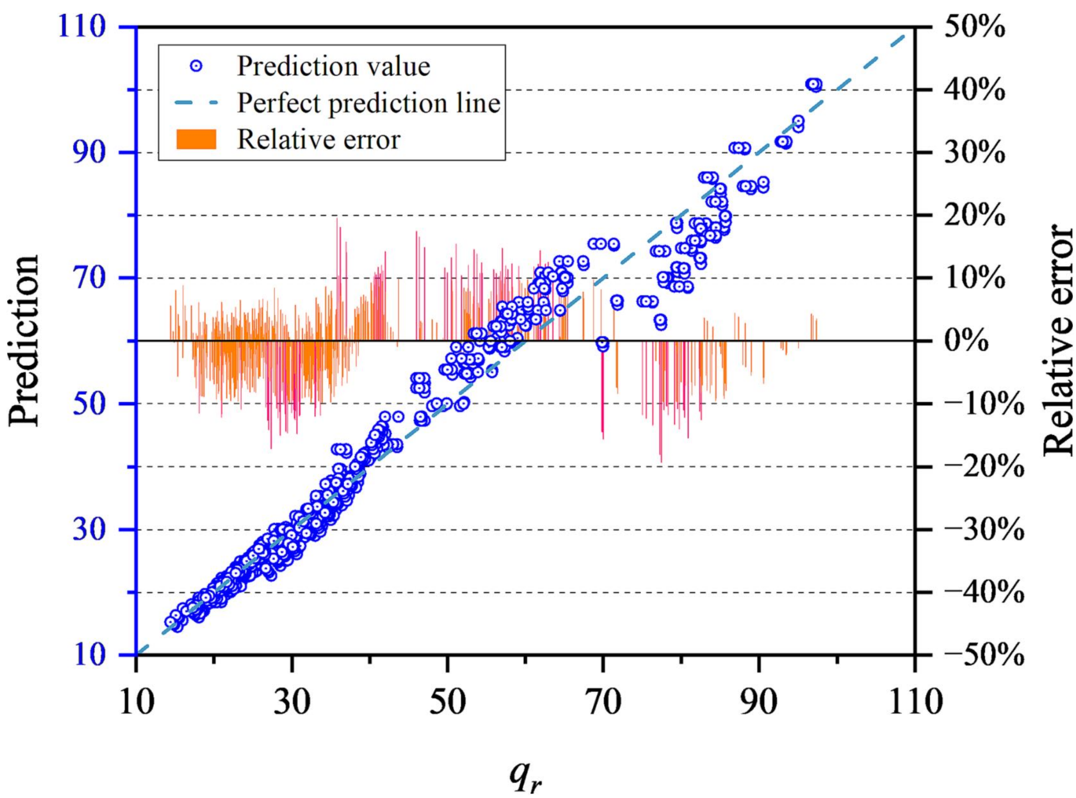

Fig. 9. Prediction accuracy of q_r formula.

Table 4
Multiple linear regression results of I and R.

Depth (m)	Coefficient of I	Coefficient of R	Intercept	R^2
3	−0.01352	−0.03528	6.067	0.90
6	−0.00694	−0.01361	4.735	0.95
9	−0.00556	−0.00981	4.665	0.96
12	−0.00463	−0.00764	4.585	0.96

implemented, but also the effects produced at different locations. Thus, I and R which respectively represent the insulation area of the interior wall and the insulation area of the roof, are improved. Table 4 displays the results of calculating weighting coefficients of I and R using the method of multiple linear regression with a as dependent variable. To find the physical meaning of coefficient, a factor F_s derived from the shape coefficient of building is proposed, and defined as the ratio of non-radiative surface area to room volume, which reflects the heat transfer loss through non-radiative building envelope. Analysis revealed a linear relationship between coefficient of I, coefficient of R, and F_s, as shown in Eq. (9). As for the intercept in Table 4, it is observed that it decreases as the room depth increases. Both the exponential decay function and logarithmic decay function fit the intercept well. Considering the fact that coefficient a is the exponential term of Eq. (7), the function form of the decay logarithm is chosen. Finally, the functional expression of a and k are proposed as Eq. (10) and Eq. (11). Combing Eq. (7), Eq. (10) and Eq. (11) yield the value of q_r when adjusting non-radiative surface emissivity and wall insulation conditions in varying room size.

$$\begin{cases} Coefficient\ of\ I = 0.010 - 0.018F_s \\ Coefficient\ of\ R = 0.041 - 0.056F_s \end{cases} \tag{9}$$

$$a = 4.89 - 0.13ln(D - 2.9999) + (0.010 - 0.018F_s) \times I + (0.041 - 0.056F_s) \times R \tag{10}$$

$$k = -ln[3.82a + (6.07 - 1.06a)ln(D - 2.95) - 9.40] \times 10^{-9} \tag{11}$$

Table 5
Comparison of relative error.

No.	t_p(℃)	t_a(℃)	*AUST*(℃)	q_r(W/m^2)	RE of formula	RE of JGJ 142	Data source
1	19.1	26.9	21.6	41.9	−4.39 %	−33.55 %	Lu [19]
2	20.1	27.4	18.4	48.7	−8.34 %	−4.22 %	
3	22.2	29.8	22.2	36.8	7.98 %	10.43 %	
4	19.1	26.9	18.6	41.9	−4.39 %	2.51 %	
5	26.9	32	25.6	35.9	49.68 %	48.16 %	Cholewa [39]
6	28.9	34.8	27.9	40.4	8.01 %	50.24 %	
7	30.7	37.4	29.1	49.6	−28.99 %	48.03 %	
8	18.1	26	17.1*	54.9	−11.64 %	41.05 %	Wang [40]
9	18.3	29.5	16.8*	72.7	−73.40 %	60.18 %	

**AUST* value is unavailable in the original paper. For calculation purpose of JGJ 142 formula, *AUST* is treated as 1.5–2℃ cooler than t_a.

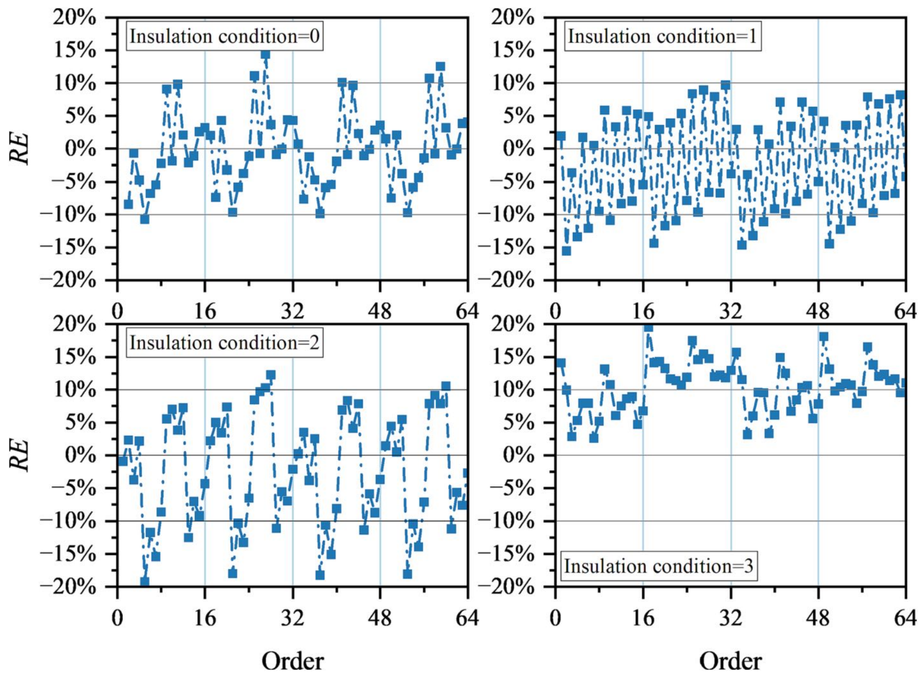

Fig. 10. *RE* contribution in 6-m-deep room.

3.3. Prediction effect analysis

In this paper, 1536 data sets are firstly used to validate the prediction accuracy of the empirical formula, and the results are shown in Fig. 9. In addition to the use of *RMSE* as the evaluation indicator, *RE* (relative error) is also used. The *RE* calculation is as follows:

$$RE = \frac{\hat{y}_i - y_i}{y_i} \tag{12}$$

The *RMSE* is 3.08, and the predicted *RE* is within 20 % with 91 % of predictions not exceeding 10 %. One of the reasons why the *RE* of 9 % of predicted results exceeds 10 % is that close *RE* is relatively distinct when absolute value q_r is small. To further improve prediction accuracy, the NLS method combining reliable formula structure via Section 3.2 and treating the coefficient as unidentified can be utilized. The *RMSE* of improved formula drops to 2.74, and the equations for the improved coefficients a and k are provided in Eq. (13) and Eq. (14).

$$a = 4.89 - 0.115ln(D - 2.999) + (0.010 - 0.0175F_s) \times I + (0.022 - 0.0364F_s) \times R \tag{13}$$

$$k = -ln[3.96a + (6 - 0.957a)ln(D - 2.925) - 10] \times 10^{-9} \tag{14}$$

In addition to using the data presented in this paper for validation, we employ data from publicly available publications, and compare the results with JGJ 142 formula [7]. The validation results of validation are displayed in Table 5. There are few papers examining the energy-saving benefits of low-emissivity surfaces on RAC, and the majority of them lack formula-required data. In Table 5, the depth of the testing room ranges between 3 and 5 m. The accuracy of the formula proposed in this paper is greater than that of *JGJ 142* formula, with a prediction error of no more than 10 % for a total of 5 sets of data, whereas *JGJ 142* formula includes only 2 sets. Both formulas produce comparable results for the fifth data set, but deviate significantly from the actual data source. Due to the difficulty of achieving steady-state heat transfer in laboratory and the inability to directly measure q_r, it is believed that the fifth original paper's measurement may contain errors. The 7–8th data sets indicate that our formula tends to underestimate q_r, whereas *JGJ 142* formula overestimates it. The identical scenario can be found in Fig. 9. Actual q_r increases as room depth decreases, while the formula tends to be underestimated q_r when it is large. Consequently, modifications are possible for rooms with shallower depths.

Observation has revealed that the error exhibits a certain pattern. Fig. 10 depicts *RE* distribution for various insulation conditions using a 3-meter-deep room as an example. The horizontal axis denotes repeatedly change in surface emissivity in 16 sets, while *RE* follows periodic

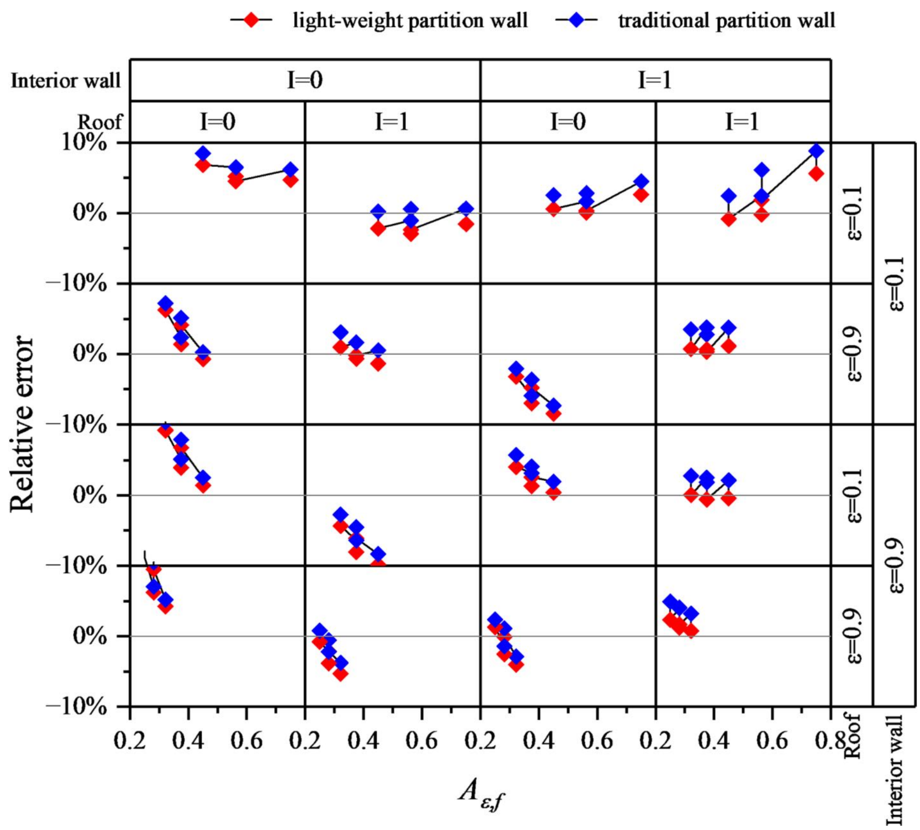

Fig. 11. Relationships between $A_{\varepsilon,f}$ and *RE*.

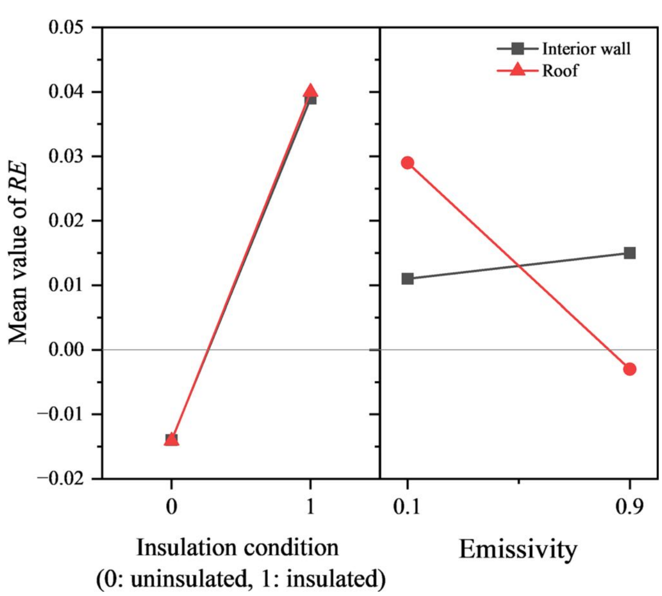

Fig. 12. Main effects of *RE*.

changes. In addition, Fig. 11 illustrates relationships between $A_{\varepsilon,f}$ and *RE* in various combination groups of envelop positions and surface emissivity. Different groups experience different levels of RE change. The main effect analysis and interaction analysis of errors under different conditions were conducted, as shown in Fig. 12 and Fig. 13, respectively. The interaction analyses reveal a clear mutual constraint relationship between wall insulation condition and surface emissivity, as the different curves are not parallel but intersect. As shown in Fig. 13, with no wall insulation and conventional surface emissivity ($\varepsilon = 0.9$) as the reference point, increasing insulation alone results in a reduction in *RE*, and reducing surface emissivity alone also results in a reduction in *RE*. However, decreasing surface emissivity and improving wall insulation simultaneously result in an increase compared to the previous two strategies. From the perspective of error variation, reducing surface emissivity can be used as one passive building energy-saving technique, just like improving wall insulation performance, yet the two may be complementary. Nonetheless, this conclusion merits further argumentation.

By analyzing data sets with significant prediction errors, it was evaluated that the prediction formula would overestimate when both wall insulation measures and the reduction of surface emissivity are taken simultaneously in the same room. If more than three walls or floors in a room with FRH satisfy the above conditions, the result of this prediction formula should be multiplied by a conservative coefficient of 0.90 for rooms with a depth less than 6 m. And Fig. 14 can be used as a guide for determining the correction factor based on the actual room size and insulation conditions.

It should be mentioned that the formula for prediction provided in this paper has preconditions for application. The data required to derive the formula was collected in a room with 6 m width and 3 m clear height. One wall is an exterior wall with an outdoor air temperature of 5 ℃, while two walls belong to household partition wall with an adjacent room temperature of 15 ℃; the final one last vertical wall is indoor partition wall. Nevertheless, there has no bearing on the prediction effect with the variation of adjacent rooms.

The steps to use the prediction formula proposed in this paper are as follows: firstly, obtain the average temperature of the floor surface through measurement or simulation; secondly, determine the indoor air temperature through measurement or design values; then, calculate the coefficients *a*, *k* in the order of Eq. (9), Eq. (13), and Eq. (14) , and finally obtain q_r by substituting *a*, *k* into Eq. (7).

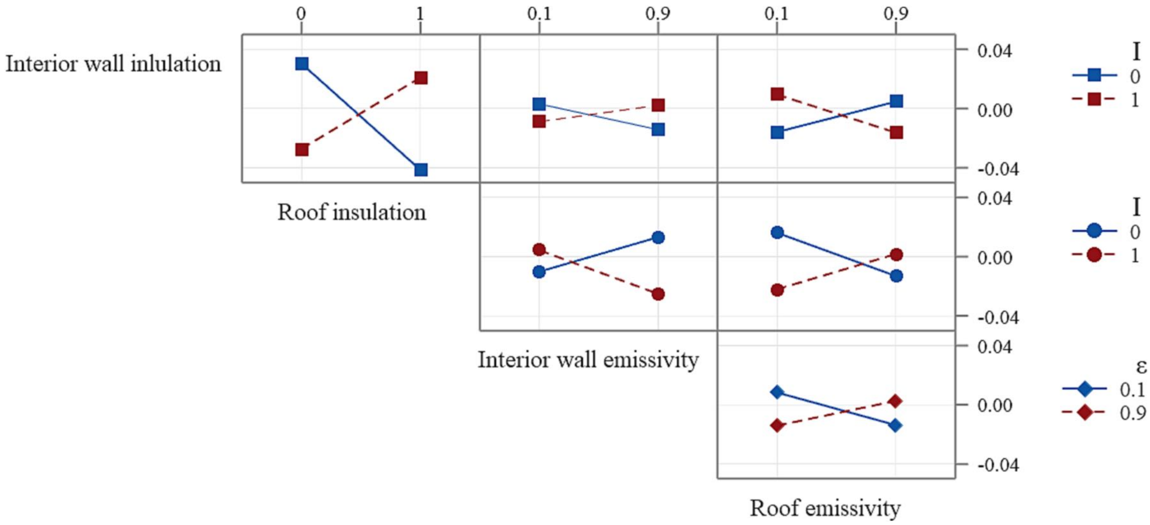

Fig. 13. Interaction analysis of *RE*.

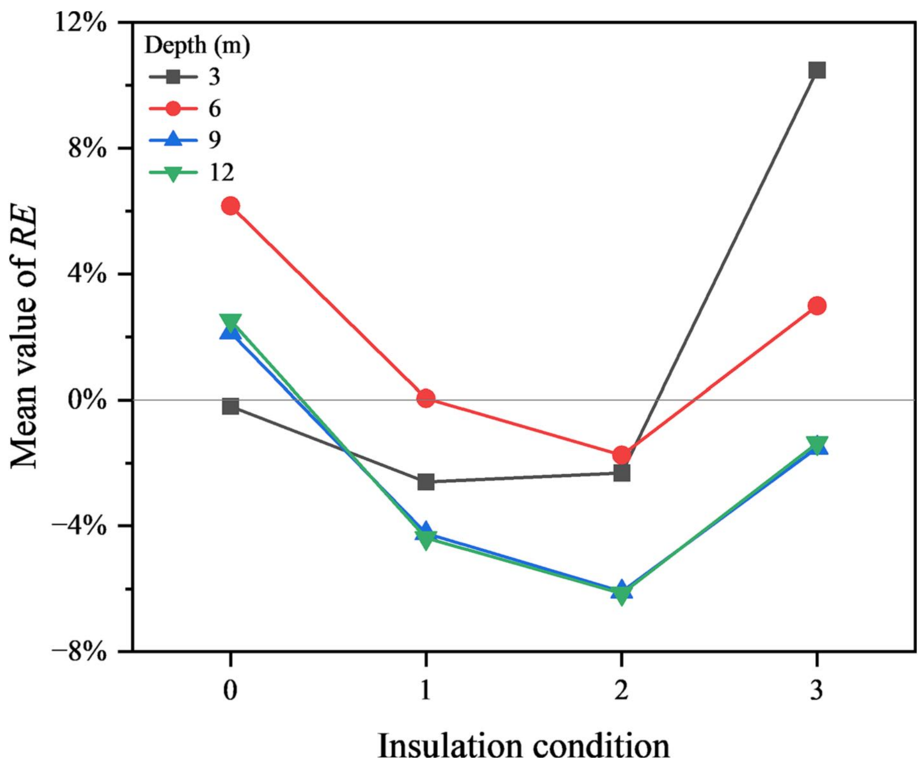

Fig. 14. Mean value under different depths and insulation conditions.

4. Discussion

4.1. Benefits of utilizing t_a rather than*AUST*

Several studies have indicated that the heat transfer effect of RAC is dependent not only on the structure and operation parameters of the terminal, but also on the building envelope structure and ambient temperature conditions [17,41]. As an intermediate node of the heat transfer process, air temperature is frequently correlated with the inner surface temperature of each wall and floor slab, and has an inherent functional relationship with the latter. When the thermal parameters of the building envelope structure are known, it can also be expressed as a function of outdoor air temperature. This can explain why utilizing t_a rather than *AUST* in the empirical formula provided for calculating the fourth power is reasonable. The temperature constraint in HVAC applications, which typically runs from 0 to 40 °C, is another factor. As demonstrated in Fig. 15, the variations of t_a and *AUST* do not exceed [20,32]. Due to the modest temperature variation, it is typical to reduce the fourth power to a linear equation, and the contributions of t_a and *AUST* in Fig. 15 also exhibit a linear relationship.

We are accustomed to using t_r as one of the variables for calculating q_r, but the improved formula presented in this paper uses t_a instead of *AUST*, which has no effect on the method's prediction effect. To discuss the difference in prediction performance between using *AUST* and t_a independently, we performed the work described in section 3.2 with *AUST* as the independent variable and derived the equivalent empirical

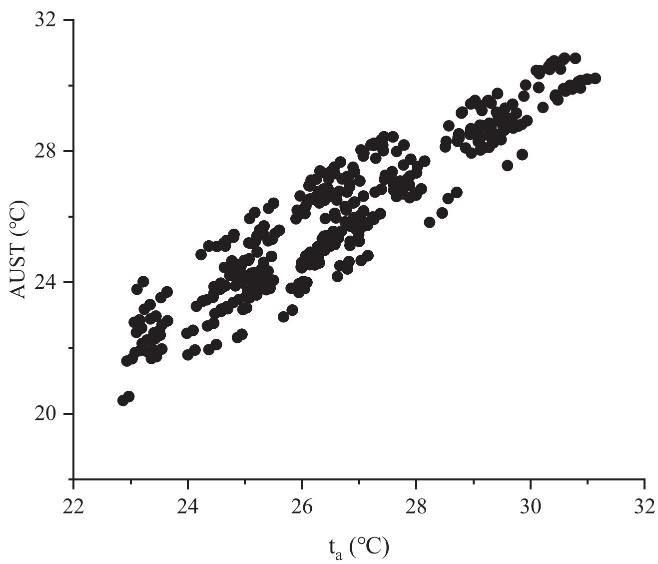

Fig. 15. Relationship between t_a and *AUST*.

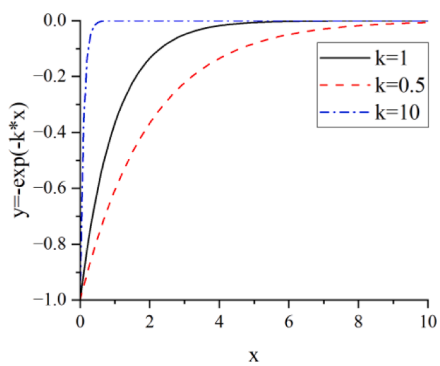

Fig. 16. Negative exponential curves under different *k* values.

Table 6
Value of a under different average air speed.

Average air speed	<0.2 m/s	0.2 to 0.6 m/s	0.6 to 1.0 m/s
a	0.5	0.6	0.7

Table A1
Overview table of independent variable settings.

Variable name	Contents	Number of levels	Notes
Surface emissivity	0.1, 0.9	2	Combined with emissivity, insulation and setting position, there are $2^4 \times 4 =$ 64 groups.
Surface location	Exterior wall, interior wall, roof, partition wall	4	
Room size	3 m,6m,9m, 12 m (Depth)	4	
Wall insulation method	Interior wall, roof, partition wall	4	
Total number of simulation		256	

formula. R^2 of the empirical formula is 0.81, and *RMSE* is 7.35, which is 2.4 times greater than *RMSE* of the formula using t_a. This suggests that when using formulas with the same structure for prediction, t_a is preferable to *AUST*. This may be because the formula structure derived in this paper is more suitable for t_a, as *AUST* is also the result of simplified calculations.

Using t_a instead of *AUST* has the most obvious benefit of reducing measuring requirements. As indicated previously, although *AUST* has a clear method of computation, it requires measuring the temperature of each inner surface, which necessitates additional measurement equipment and undoubtedly increases the measurement system's complexity. In addition, several researchers have discovered issues with different calculating methods when the surface emissivity varies [17,42,43]. In contrast, the air temperature measurement method is mature and straightforward, and the air temperature has been a control parameter for HVAC equipment for decades. Utilizing t_a rather than *AUST* makes incorporating the formula into the control system more foreseeable and practical.

4.2. Limitations of q_r as selection criteria

Calculating the heat flow rate of radiant surface allows the selection of the RAC terminal capable of meeting heating requirements, as well as the verification of the minimum radiant surface area. The purpose of the lookup table in JGJ142 is to facilitate the equipment lectotype for designers, despite the fact that its calculation condition puts the supply and return water temperature difference at 10 °C. Nevertheless, depending exclusively on these design indicators is inadequate.

In order to make the operation of air conditioning more energy-efficient, researchers are increasingly recognizing the intermittent operating mode in HVAC industry [10,44,45]. However, q_r is a static indicator and cannot represent the dynamic performance of FRH. Due of its structural properties, the FRH's temperature response time is relatively slow. Despite the fact that lightweight RFH has been designed to explore the idea of repaid response ability [40,46], its effect is not equal to that of conventional convective air cooling (AC) due to the "ineffective heat" presented by Zhe [47]. Numerous studies are therefore focused on reducing the response time of the RAC during intermittent operation. The response curve of the RAC is proved as a negative exponential function based on Euler number [48,49]. As time approaches infinity, heat transfer reaches a steady state when it can be characterized with heat flow rate of radiant surface. Nevertheless, as shown in Fig. 16, even if the steady-state heat transfer is the same when *k* value is varied, the early increase in the curve differs dramatically. The faster the response speed, the bigger *k*'s value. Therefore, it is vital to develop indicators capable of describing the dynamic reaction process of RAC and to investigate the possibility of the building envelop construction to reduce response time.

4.3. The importance of inner surfaces involved in radiation

The surface of an object serves as the medium for radiant heat transfer, and the object's surface area, relative position, and emissivity have significant effects on the radiant heat transfer process. The Stefan-Boltzmann law is the basic basis for applying radiant heat transfer theory to air conditioning. As stated in section 4.2, radiant heat transfer is approximated linearly in engineering due to the small temperature difference in comparison to the change amplitude of several hundred Kelvin degrees. And radiant heat transfer is often not addressed in AC applications due to the tiny temperature difference between surfaces. Unlikely, the energy-saving potential of radiant heat transfer must be considered, as radiant heat transfer accounts for more than 50 % of RAC's heat exchange [50]. The inner surface of the building envelopes serves as the heat transfer medium for RAC, and its surface characteristics can influence the heat transfer impact. Using the calculation of operating temperature t_o as an example, the mean radiant temperature *MRT* accounts for surface temperatures and simplifies the area-weighted computation of view factors [51]. The calculating method is denoted by Eq. (10), and the value of *a* can be chosen according to Table 6. But assuming $a = 0.5$ and $MRT = t_a$ frequently occur in engineering practice

Table A2
Table of envelope parameters.

Structure	Component	Thermal conductivityW/(m·K)	Density kg/m^3	Specific heat capacityJ/(kg·K)	Thickness m
Wall with external insulation	Cement mortar	0.93	1800	1050	0.01
	EPS board	0.04	18	2414.8	0.03
	concrete block	0.57	1700	1782	0.2
Wall with internal insulation	Cement mortar	0.93	1800	1050	0.01
	Concrete block	0.57	1700	1782	0.2
	EPS board	0.04	18	2414.8	0.03
Roof	Reinforced concrete	1.61	2436	929	0.1

Note: Arrange in order from inside out.

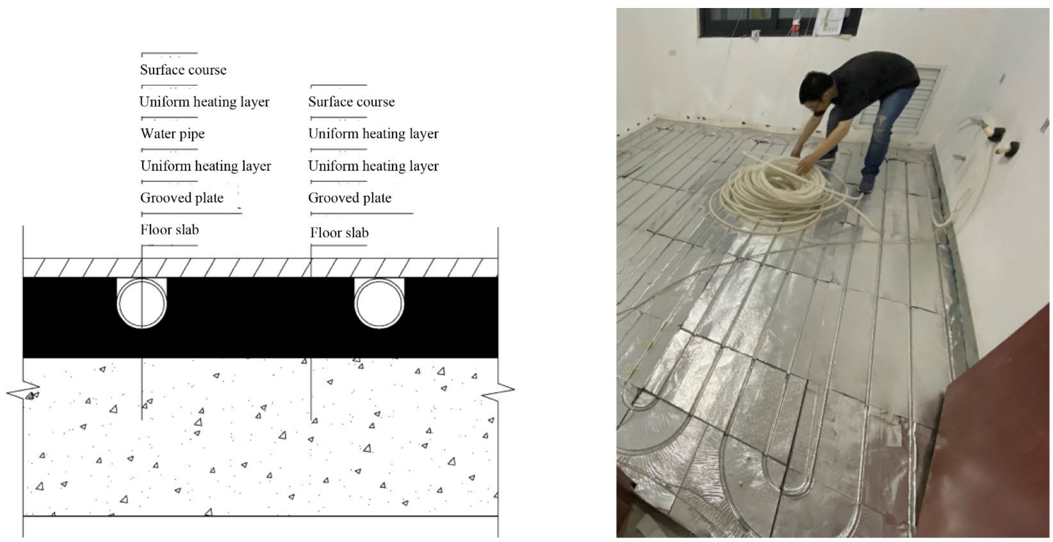

(a) Structure of one kind of lightweight FRH (b) Installation site of prefabricated groove plate

Fig. A1. Prefabricated grooved floor radiant heating.

Table A3
Table of Prefabricated grooved FRH parameters.

Structure and layer	Material	Thermal conductivityW/(m·K)	Density kg/m^3	Specific heat capacityJ/(kg·K)	Thickness m
Surface course	Wood floor	0.14	500	2510	0.012
Uniform heating layer	Aluminum foil	237	2702	903	0.0002
Water pipe	PE-RT	0.40	933	2100	0.002
Grooved plate	Foam concrete	0.12	475	1050	0.04

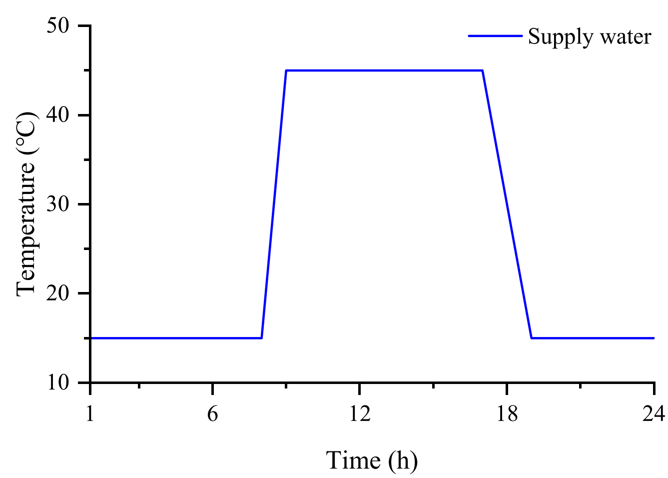

Fig. A2. Floor radiant heating operation schedule.

that lacks measurements to probe air velocity and temperature of each surface, which may lead to a misunderstanding of radiant heat transfer [43,52].

$$t_o = at_a + (1-a)MRT \tag{15}$$

It is promising that researchers have continuously devised and implemented building envelopes to enhance RAC's operational efficiency. Airport applications have demonstrated the superiority of RAC in large space buildings, which will surely hasten its adoption in public buildings. In addition, the advancement of infrared temperature sensing technology enables more efficient use of surface temperature in energy-saving engineering [22,53,54]. And in recent years, research on inner surface emissivity has revealed that this measure has the potential to become another passive energy-saving technique. The authors are expecting that with the development of infrared temperature sensing technology, progress in low emissivity surface and material research, RAC achieves further development and implementation.

5. Conclusions

This paper reports the limits of existing formula for predicting the radiant heat flow rate of radiant surfaces of floor radiant heating (q_r) in the presence of varying room space and non-radiative surface emissivity. Using machine learning techniques, a prediction model was developed, and backward selection method was used to identify the requisite relevant features. In addition, an improved empirical formula for predicting q_r has been developed, and error analysis has been performed. These are the principal findings of this paper:

1) 12.5 % of the 1024 datasets with room depths of 3 m, 6 m, and 12 m were used as internal test sets to train machine learning models for predicting q_r. An additional 512 datasets with room depth of 9 m were prepared as the test set to evaluate the quality of the models. With *RMSE* values of 0.68 and 0.21 in both test sets, two-layer Neural Networks (NN) model performs well and has a shorter training time. The validation at the depth of 9 m demonstrates that the two-layer NN model has superior generalizability and performance with unknown data.
2) The substitution of *AUST* by indoor air temperature for predicting q_r has considerable accuracy. The necessary features are therefore room depth, the weighted coefficient of radiant surface area, indoor air temperature, and the average temperature of the radiant surface.
3) An empirical prediction formula adopting indoor air temperature as one of variables with the R-squared of 0.97 and *RMSE* of 2.74 was developed, suggesting a high level of prediction accuracy. The enhanced empirical formula can be used to anticipate various room space and scenarios of non-radiative surface emissivity and wall insulation conditions.
4) The distribution pattern of errors under different room depth, insulation conditions and emissivity of non-radiative surface has been investigated through analysis, so it is possible to set correction coefficients based on various circumstances. From the perspective of error analysis, low emissivity non-radiative surface has the potential to serve as passive energy-saving technique comparable to wall insulations, and merit further study.

Declaration of Competing Interest

The authors declare that they have no known competing financial interests or personal relationships that could have appeared to influence the work reported in this paper.

Data availability

Data will be made available on request.

Acknowledgements

This work was supported by the National Key R&D Program of China "Solutions to heating and cooling of buildings in the Yangtze River region" (No. 2016YFC0700303).

Appendix A:. Experimental configuration of data set

The experimental independent variables consist of the location and area of unheated surfaces, the room size, and the method of wall insulation. The emissivity of the floor is set to 0.9, whereas the emissivity of other unheated surfaces vary at two levels. According to their relative positions, unheated surfaces are divided into four types of walls: exterior wall, interior wall, partition wall and roof, because they have different temperature boundary conditions in the winter, which may influence the effect of different surface emissivity.

Considering the common room sizes and construction modulus in residential buildings, the ratio of depth to width is set at 1:2, 1:1, and 2:1, with depths of 3 m, 6 m, and 12 m correspondingly. Additional data for testing is set to a depth of 9 m separately.

The settings of independent variables are shown in Table A1.

The established object includes FRH and building envelope structure. The room is composed entirely of a non-transparent building envelope; the parameters are listed in Table A2. The structure of FRH is depicted in Fig. A1 (a), and the thermophysical properties of each structural layer are listed in Table A3.

The boundary condition outside the exterior wall is the third kind, with the simulated outdoor temperature of 5 °C and the convective heat transfer coefficient of 8.7 W/(m^2·K). The boundary condition outside the interior wall is simulated to be adjacent to a non-heating room with the temperature of 15 °C and the convective heat transfer coefficient of 6 W/(m^2·K); The boundary condition outside the floor is also 15 °C with the convective heat transfer coefficient of 4 W/(m^2·K).

As depicted in Fig. A2, a step change is constructed on the supply water side. The cycle length is 24 h, the step size is 0.5 h, and the flow rate is 1 m/s. The temperature variations within the radiant air-conditioned room and the surface heat flow variations of each wall are recorded and analyzed within 9 h. Simultaneously, steady-state simulations with a constant 45 °C supply water temperature are conducted to analyze the relationship between dynamic response characteristics and steady-state values.

References

[1] Z. Pang, Y. Chen, J. Zhang, Z. O'Neill, H. Cheng, B. Dong, Nationwide HVAC energy-saving potential quantification for office buildings with occupant-centric controls in various climates, Appl. Energy. 279 (2020), 115727, https://doi.org/10.1016/j.apenergy.2020.115727.

[2] A. Sadeghianjahromi, C.-C. Wang, Heat transfer enhancement in fin-and-tube heat exchangers – a review on different mechanisms, Renew. Sustain. Energy Rev. 137 (2021), 110470, https://doi.org/10.1016/j.rser.2020.110470.

[3] A. Hesaraki, S. Holmberg, Energy performance of low temperature heating systems in five new-built Swedish dwellings: a case study using simulations and on-site measurements, Build. Environ. 64 (2013) 85–93, https://doi.org/10.1016/j.buildenv.2013.02.009.

[4] Lu J., Wang D., Zhao K., Liu S., Experimental performance of intermittent space heating with different terminals in a self-thermal insulation building, J. Zhejiang Univ. Eng. Sci. 54 (2020) 2092-2099+2108. https://doi.org/10.3785/j.issn.1008-973X.2020.11.004.

[5] W. Liao, J. Peng, Y. Luo, Y. He, N. Li, A. Yongga, Comparative study on energy consumption and indoor thermal environment between convective air-conditioning terminals and radiant ceiling terminals, Build. Environ. 209 (2022), 108661, https://doi.org/10.1016/j.buildenv.2021.108661.

[6] ASRHAE, ASHRAE Handbook 2020: HVAC Systems and Equipment, America, 2020.

[7] MHURD, Technical specification for radiant heating and cooling, 2012.

[8] F. Cheng, X. Zhang, X. Su, Thermal performance analysis of internal and external insulation for exterior walls of residential buildings in hot summer and cold winter zone, J. Tongji Univ. Nat. Sci. 45 (2017) 827-832+860. https://doi.org/10.11908/j.issn.0253-374x.2017.06.006.

[9] F. Cheng, X. Zhang, D. Zhao, M. Zhai, Influence of external wall thermal insulation on public building air conditioning energy consumption in hot summer and colde winter area, Build. Sci. 32 (2016) 77–81, https://doi.org/10.13614/j.cnki.11-1962/tu.2016.02.13.

[10] X. Meng, T. Luo, Y. Gao, L. Zhang, X. Huang, C. Hou, Q. Shen, E. Long, Comparative analysis on thermal performance of different wall insulation forms under the air-conditioning intermittent operation in summer, Appl. Therm. Eng. 130 (2018) 429–438, https://doi.org/10.1016/j.applthermaleng.2017.11.042.

[11] F. Ruan, Theoretical Research on Envelop Insulation Effect for Residential Buildings with Compartmental and Intermittent Energy Consuming Method, Zhejiang University, 2017. Doctoral dissertation.

[12] S. Liu, K. Zhao, J. Ge, Optimal thickness of internal insulation layers in hot summer and cold winter zone with intermittent radiant floor heating, Archit. Cult. (2020) 184–185, https://doi.org/10.19875/j.cnki.jzywh.2020.11.064.

[13] D. Cvetković, M. Bojić, Optimization of thermal insulation of a house heated by using radiant panels, Energy Build. 85 (2014) 329–336, https://doi.org/10.1016/j.enbuild.2014.09.043.

[14] Y. Xiao, T. Jiang, C. Jiang, Temperature field distribution characterization of embedded air conditioning terminal heating room in different scenarios, J. Chongqing Univ. 45 (2022) 141–147, https://doi.org/10.11835/J.ISSN.1000-582X.2022.528.

[15] M. Ibrahim, L. Bianco, O. Ibrahim, E. Wurtz, Low-emissivity coating coupled with aerogel-based plaster for walls' internal surface application in buildings: energy saving potential based on thermal comfort assessment, J. Build. Eng. 18 (2018) 454–466, https://doi.org/10.1016/j.jobe.2018.04.008.

[16] S. Lu, Q. Meng, L. Zhang, K. Zhong, L. Shao, Effect of the inner wall surface radiation rate on the indoor thermal comfort, J. Build. Energy Effic. 47 (2019) 98–104, https://doi.org/10.3969/j.issn.1673-7237.2019.09.020.
[17] B. Hu, J. Chen, R. Yao, C. Du, Y. Zhu, D. Guo, Calculation methods of indoor mean radiant temperature of floor radiant cooling system and effect of surface emissivity, HV&AC. 50 (2020) 34-41+25.
[18] I. Maori, A. Hideo, Y. Yasusei, Effects Of Low Emissivity Interior Surfaces On Thermal Environment (Part 1) : Measurements On Internal Thermal Environment With Radiant Heating Using Real-Size Experimental Rooms, 日本建築学会環境系論文集. 86 (2021) 701–707. https://doi.org/10.3130/aije.86.701.
[19] L. Lidi, J. Chen, S. Tao, X. Liu, H. Yaqi, Q. Luo, L. Luo, An RC-network model in the frequency domain for radiant floor heating coupled with envelopes, Build. Environ. (2022), 109617, https://doi.org/10.1016/j.buildenv.2022.109617.
[20] K. Zhao, X.-H. Liu, Y.i. Jiang, On-site measured performance of a radiant floor cooling/heating system in Xi'an Xianyang International Airport, Sol. Energy. 108 (2014) 274–286, https://doi.org/10.1016/j.solener.2014.07.012.
[21] K. Zhao, X.-H. Liu, Y. Jiang, Application of radiant floor cooling in large space buildings – a review, Renew. Sustain. Energy Rev. 55 (2016) 1083–1096, https://doi.org/10.1016/j.rser.2015.11.028.
[22] Y. Zhang, C. Zhao, T. Olofsson, G. Nair, B. Yang, A. Li, Field measurements and numerical analysis on operating modes of a radiant floor heating aided by a warm air system in a large single-zone church, Energy Build. 255 (2022), 111646, https://doi.org/10.1016/j.enbuild.2021.111646.
[23] M. Wang, Q. Zhao, Y. Chen, Study on heat load calculation of radiant floor heating room, Build. Sci. 36 (2020) 169–177, https://doi.org/10.13614/j.cnki.11-1962/tu.2020.04.25.
[24] P.W. Tien, S. Wei, J. Darkwa, C. Wood, J.K. Calautit, Machine learning and deep learning methods for enhancing building energy efficiency and indoor environmental quality – a review, Energy AI. 10 (2022), 100198, https://doi.org/10.1016/j.egyai.2022.100198.
[25] Z. Chen, F. Xiao, F. Guo, J. Yan, Interpretable machine learning for building energy management: A state-of-the-art review, Adv. Appl. Energy. 9 (2023), 100123, https://doi.org/10.1016/j.adapen.2023.100123.
[26] Q. Zhang, Y. Huang, C.-B. Chng, C.-K. Chui, P.-S. Lee, Investigations on machine learning-based control-oriented modeling using historical thermal data of buildings, Build. Environ. 243 (2023), 110595, https://doi.org/10.1016/j.buildenv.2023.110595.
[27] L.C.M. Dafico, E. Barreira, R.M.S.F. Almeida, R. Vicente, Machine learning models applied to moisture assessment in building materials, Constr. Build. Mater. 405 (2023), 133330, https://doi.org/10.1016/j.conbuildmat.2023.133330.
[28] C. Aggarwal, H. Ge, M. Defo, M.A. Lacasse, Hygrothermal performance assessment of wood frame walls under historical and future climates using partial least squares regression, Build. Environ. 223 (2022), 109501, https://doi.org/10.1016/j.buildenv.2022.109501.
[29] G. Zhang, Y. Ge, A. Khudhair Yakoob, T. Alkhalifah, F. Alturise, H. Elhosiny Ali, Y. Yang, Determining the heat transfer coefficient of sustainable buildings using extreme learning machine, Fuel. 336 (2023), 126795, https://doi.org/10.1016/j.fuel.2022.126795.
[30] A. Royuela-del-Val, M.Á. Padilla-Marcos, A. Meiss, P. Casaseca-de-la-Higuera, J. Feijó-Muñoz, Air infiltration monitoring using thermography and neural networks, Energy Build. 191 (2019) 187–199, https://doi.org/10.1016/j.enbuild.2019.03.019.
[31] Z. Shen, S. Shrestha, D. Howard, T. Feng, D. Hun, B. She, Machine learning–assisted prediction of heat fluxes through thermally anisotropic building envelopes, Build. Environ. 234 (2023), 110157, https://doi.org/10.1016/j.buildenv.2023.110157.
[32] Q. Chen, N. Li, Thermal response time prediction-based control strategy for radiant floor heating system based on Gaussian process regression, Energy Build. 263 (2022), 112044, https://doi.org/10.1016/j.enbuild.2022.112044.
[33] J.-A. Goulet, Probabilistic Machine Learning for Civil Engineers, MIT Press, 2020.
[34] L. Breiman, Classification and Regression Trees, Routledge, New York, 2017, 10.1201/9781315139470.
[35] Z. He, G. Liu, X. Zhao, M. Wang, Overview of Gaussian process regression, Control Decis. 28 (2013) 1121-1129+1137. https://doi.org/10.13195/j.kzyjc.2013.08.018.
[36] P.M. Van Every, M. Rodriguez, C.B. Jones, A.A. Mammoli, M. Martínez-Ramón, Advanced detection of HVAC faults using unsupervised SVM novelty detection and Gaussian process models, Energy Build. 149 (2017) 216–224, https://doi.org/10.1016/j.enbuild.2017.05.053.
[37] S.I. Granshaw, Neural networks and neurodiversity, Photogramm. Rec. 36 (2021) 192–196, https://doi.org/10.1111/phor.12376.
[38] A. Morales-Hernández, I. Van Nieuwenhuyse, S. Rojas Gonzalez, A survey on multi-objective hyperparameter optimization algorithms for machine learning, Artif. Intell. Rev. 56 (2023) 8043–8093, https://doi.org/10.1007/s10462-022-10359-2.
[39] T. Cholewa, M. Rosiński, Z. Spik, M.R. Dudzińska, A. Siuta-Olcha, On the heat transfer coefficients between heated/cooled radiant floor and room, Energy Build. 66 (2013) 599–606, https://doi.org/10.1016/j.enbuild.2013.07.065.
[40] Y. Wang, W.u. Xiaozhou, J. Gao, A. Feng, J. Wang, D. Liu, X. Zhou, Simplified model for heat transfer and surface temperature of prefabricated radiant heating and cooling system, Energy Build. 276 (2022), 112522, https://doi.org/10.1016/j.enbuild.2022.112522.
[41] M.F. Özbey, C. Turhan, A comprehensive comparison and accuracy of different methods to obtain mean radiant temperature in indoor environment, Therm. Sci. Eng. Prog. 31 (2022), 101295, https://doi.org/10.1016/j.tsep.2022.101295.
[42] F. Frontini, T.E. Kuhn, The influence of various internal blinds on thermal comfort: A new method for calculating the mean radiant temperature in office spaces, Energy Build. 54 (2012) 527–533, https://doi.org/10.1016/j.enbuild.2012.02.029.
[43] H. Guo, D. Aviv, M. Loyola, E. Teitelbaum, N. Houchois, F. Meggers, On the understanding of the mean radiant temperature within both the indoor and outdoor environment, a critical review, Renew. Sustain. Energy Rev. 117 (2020), 109207, https://doi.org/10.1016/j.rser.2019.06.014.
[44] D. Chenqiu, B. Li, Y. Wei, H. Liu, R. Yao, Energy flexibility for heating and cooling based on seasonal occupant thermal adaptation in mixed-mode residential buildings, Energy. 189 (2019), 116339, https://doi.org/10.1016/j.energy.2019.116339.
[45] H. Jiang, R. Yao, S. Han, D. Chenqiu, Y. Wei, S. Chen, B. Li, Y. Hang, N. Li, J. Peng, B. Li, How do urban residents use energy for winter heating at home? A Large-Scale Survey in the Hot Summer and Cold Winter Climate Zone in the Yangtze River Region, Energy Build. 223 (2020), 110131, https://doi.org/10.1016/j.enbuild.2020.110131.
[46] Y. Fang, X. Zhang, C. Liu, Experimental study of lightweight radiant floor heating system with non-full-coverage heat-conducting plate, J. Southeast Univ. Nat. Sci. Ed. 52 (2022) 1104–1113, https://doi.org/10.3969/j.issn.1001-0505.2022.06.010.
[47] Z. Wang, M. Luo, Y. Geng, B. Lin, Y. Zhu, A model to compare convective and radiant heating systems for intermittent space heating, Appl. Energy. 215 (2018) 211–226, https://doi.org/10.1016/j.apenergy.2018.01.088.
[48] J. Lin, C. Chen, Y. Ma, L. Sun, Calculated model of hot water radiant floor stable heating process, Acta Energiae Solaris Sin. 40 (2019) 914–920, https://doi.org/10.19912/j.0254-0096.2019.04.004.
[49] Y. Wang, X. Wu, J. Gao, J. Wang, D. Liu, A. Feng, X. Zhou, Test Method of dynamic thermal performance of prefabricated floor radiant terminals, Build. Sci. 38 (2022) 65–71, https://doi.org/10.13614/j.cnki.11-1962/tu.2022.10.09.
[50] K.-N. Rhee, K. Woo Kim, A 50 year review of basic and applied research in radiant heating and cooling systems for the built environment, Build. Environ. 91 (2015) 166–190, https://doi.org/10.1016/j.buildenv.2015.03.040.
[51] ASHRAE, Standard 55-Thermal environmental conditions for human occupancy, 2017.
[52] E. Halawa, J. van Hoof, V. Soebarto, The impacts of the thermal radiation field on thermal comfort, energy consumption and control—a critical overview, Renew. Sustain. Energy Rev. 37 (2014) 907–918, https://doi.org/10.1016/j.rser.2014.05.040.
[53] M.-S. Shin, K.-N. Rhee, G.-J. Jung, Optimal heating start and stop control based on the inferred occupancy schedule in a household with radiant floor heating system, Energy Build. 209 (2020), 109737, https://doi.org/10.1016/j.enbuild.2019.109737.
[54] X. Zhou, Y. Liu, J. Zhang, L. Ye, M. Luo, Radiant asymmetric thermal comfort evaluation for floor cooling system – a field study in office building, Energy Build. 260 (2022), 111917, https://doi.org/10.1016/j.enbuild.2022.111917.